

An Extension of Clarke's Model With Stochastic Amplitude Flip Processes

Håkon Hoel and Henrik Nyberg

Abstract—Stochastic modeling is an essential tool for studying statistical properties of wireless channels. In multipath fading channel (MFC) models, the signal reception is modeled by a sum of wave path contributions, and Clarke's model is an important example of such which has been widely accepted in many wireless applications. However, since Clarke's model is temporally deterministic, Feng and Field noted that it does not model real wireless channels with time-varying randomness well. Here, we extend Clarke's model to a novel time-varying stochastic MFC model with scatterers randomly flipping on and off. Statistical properties of the MFC model are analyzed and shown to fit well with real signal measurements, and a limit Gaussian process is derived from the model when the number of active wave paths tends to infinity. A second focus of this work is a comparison study of the error and computational cost of generating signal realizations from the MFC model and from its limit Gaussian process. By rigorous analysis and numerical studies, we show that in many settings, signal realizations are generated more efficiently by Gaussian process algorithms than by the MFC model's algorithm. Numerical examples that strengthen these observations are also presented.

Index Terms—Multipath channels, Gaussian processes, ray tracing.

I. INTRODUCTION

IN radio communication settings with a fixed transmitter, Clarke's model [3] for a wireless flat fading channel may be expressed by

$$\xi_{t,M} = \frac{1}{\sqrt{M}} \sum_{m=1}^M e^{-i(2\pi f_c v \cos(\alpha_m)t/c + \theta_m)}, \quad (1)$$

where v denotes speed of the receiver, f_c the carrier frequency, $\{\theta_m\}_{m=1}^M$ are i.i.d. initial phase shifts, $\theta_m \sim U[0, 2\pi)$, and α_m is the arrival angle of the m th component wave, distributed according to a scatterer density $p(\alpha)$. When the scatterer density is a constant, Clarke noted that the autocorrelation function $E[\xi_{t,M} \xi_{0,M}^*]$ converges to the zeroth-order Bessel function of

Manuscript received May 14, 2013; revised November 10, 2013 and April 23, 2014; accepted May 23, 2014. Date of publication June 4, 2014; date of current version July 18, 2014. This work was supported in part by the Center for Industrial and Applied Mathematics at the Royal Institute of Technology (KTH) and in part by the King Abdullah University of Science and Technology Strategic Research Initiative Center for Uncertainty Quantification in Computational Science. The associate editor coordinating the review of this paper and approving it for publication was O. Oyman.

H. Hoel is with the Division of Mathematics, King Abdullah University of Science and Technology, Thuwal 23955-6900, Saudi Arabia, and also with the Department of Numerical Analysis and Computer Science, Royal Institute of Technology (KTH), 100 44 Stockholm, Sweden (e-mail: hakon.hoel@kaust.edu.sa).

H. Nyberg is with Ericsson AB, 164 80 Stockholm, Sweden (e-mail: Henrik.L.Nyberg@ericsson.com).

Color versions of one or more of the figures in this paper are available online at <http://ieeexplore.ieee.org>.

Digital Object Identifier 10.1109/TCOMM.2014.2328595

the first kind $J_0(2\pi f_c vt/c)$ as $M \rightarrow \infty$, and that the signal's power spectral density (PSD) takes the form of Jakes' spectrum:

$$S(f) = \begin{cases} \frac{1}{\pi\sqrt{f_D^2 - f^2}}, & \text{if } |f| < f_D \\ 0, & \text{else,} \end{cases} \quad (2)$$

with $f_D = v f_c / c$ denoting the maximum Doppler frequency shift. Feng and Field [4] observed two shortcomings of Clarke's model. First, in settings where the receiver is standing still, i.e., $v = 0$, the received signal $\xi_{t,M}$ in (1) will be constant, but, in contrast, received signals in real wireless channel environments will fluctuate even when the receiver is standing still. Second, the PSD of real signal measurements tend to deviate from the U-shape of Jakes' spectrum by having a wider support than $[-f_D, f_D]$, cf. [4, Fig. 4] and Fig. 4. It should be clear from these shortcomings of Clarke's model that extensions are necessary to model real wireless channels with time-varying randomness accurately. For this purpose, Feng and Field proposed the following extension of Clarke's model that incorporates the effect of fluctuations in the component phases:

$$\varepsilon_t = \sum_{m=1}^M a_m \exp\left(i\left(2\pi f_n t + \phi_t^{(m)}\right)\right). \quad (3)$$

Here, the amplitudes a_m are i.i.d. random variables, $f_n = f_D \cos(\alpha_m)$ are the Doppler shifts, and the phases $\phi_t^{(m)}$ are independent Wiener processes with uniform initial distribution in $[0, 2\pi)$

$$d\phi_t^{(m)} = \sqrt{B}dW_t^{(m)}, \quad \phi_0^{(m)} \sim U[0, 2\pi), \quad (4)$$

where B is a constant with the dimension of frequency. See also [5] for an asymptotic study, as $M \rightarrow \infty$, for a closely related MFC model with Wiener process driven phase components.

In this paper, we propose an alternative MFC model for addressing the shortcomings of Clarke's model that incorporates time-varying randomness through stochastic amplitude processes a_m that flip on and off. Our proposed MFC model is motivated from the assumption that time-varying randomness derives from the appearance and disappearance of wave paths in the scattering environment. Furthermore, by analyzing the asymptotics when the number of active wave paths tends to infinity, we derive through rigorous analysis that signal realizations of our proposed MFC model converge in distribution to a Gaussian process.

When studying a channel model statistically by means of sample averages of numerical signal realizations, numerical error and computational cost are important issues to consider. To control the bias in your estimates it is important to

TABLE I
 COMPUTATIONAL COST IN GENERAL MODEL SETTINGS

	Computational cost
Algorithm 1	$\mathcal{O}\left(L \text{TOL}^{-2} \left(\frac{N^{3/2}}{S_N}\right)^3\right)$
Algorithm 2	$\mathcal{O}\left(N^3 + N^2 \left(\frac{N^{3/2}}{S_N \text{TOL}}\right)^{1/\gamma} + LN^2\right)$

 TABLE II
 COMPUTATIONAL COST IN THE WSS SETTING (14)

	Computational cost
Algorithm 1	$\mathcal{O}\left(L \text{TOL}^{-2} \left(\frac{N^{3/2}}{S_N}\right)^3\right)$
Algorithm 2	$\mathcal{O}\left(N^3 + N \left(\frac{N^{3/2}}{S_N \text{TOL}}\right)^{1/\gamma} + LN^2\right)$
Algorithm 3	$\mathcal{O}\left(N \left(\frac{N^{3/2}}{S_N \text{TOL}}\right)^{1/\gamma} + LN \log(N)\right)$

generate numerical signal realizations as accurately as possible, and to control the statistical error it is important to generate sufficiently many samples. Another contribution of this paper is a cost and accuracy study of generating numerical signal realizations of our proposed MFC model. A signal realization error measure is introduced and the presented algorithms are studied in terms of accuracy and computational cost. The results are summarized in Tables I and II, and from these results we conclude that in many settings the Gaussian process algorithms generate signal realizations more efficiently than the MFC algorithm. Numerical examples corroborate the cost and accuracy observations, and one numerical example illustrating properties of the Gaussian process model in a time-varying reflection environment is also given.

The rest of this paper is organized as follows. In Section II we present our MFC model extension of Clarke's model and a numerical algorithm for generating signal realizations from the MFC model. In Section III we derive that when the number of active wave paths in the MFC model tends to infinity, the output signal converges in distribution to a Gaussian process. Furthermore, two algorithms for generating Gaussian process signal realizations are presented, and an error and complexity analysis of all the algorithms is given. In Section IV we investigate the relation between the signal's autocorrelation and PSD for wide-sense stationary (WSS) settings and describe a method for estimating the flip rate and scatterer density from PSD measurements. Section V provides numerical examples that illustrate various statistical properties of the developed model with comparisons to real measurement data, and thereafter we close the paper with concluding remarks.

II. THE EXTENDED CHANNEL MODEL

In this section we propose an extension of Clarke's model that incorporates the birth and death of wave paths through stochastic amplitude processes flipping on and off. A numerical algorithm for generating realizations of the proposed MFC model is also presented.

A. Model Description

We consider a channel environment with a fixed transmitter and the receiver moving with a constant speed in an urban environment with buildings obstructing the line of sight between

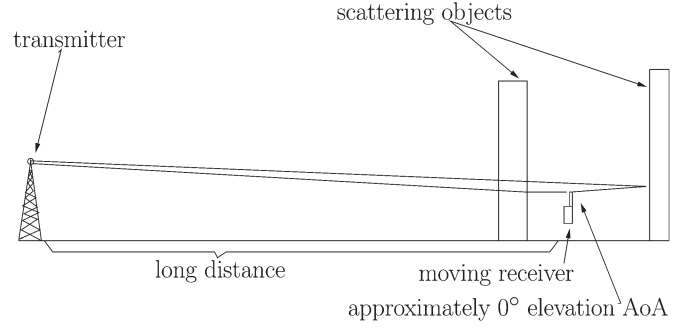


Fig. 1. Illustration of a typical wireless channel scattering environment for our MFC model.

scatterer and receiver. The incoming rays are modeled as scattered off the receiver's surroundings with the majority of scattering surfaces assumed to be flat walls. The distance between transmitter and receiver is assumed so large that it is reasonable to consider the elevation angle of arrival (AoA) of incoming wave paths to be 0° , cf. Fig. 1. That is, scatterers are assumed to lie in the horizontal plane. The received signal is modeled by

$$Z_{t,M} = \frac{1}{\sqrt{M}} \sum_{m=1}^M a(\alpha_m, t) e^{-i(2\pi f_c \tau(\alpha_m, t) + \theta_m(t))}, \quad (5)$$

where f_c denotes the carrier frequency, $\{\alpha_m\}_{m=1}^M$ are the angle of arrival of the wave paths that are i.i.d. according to a prescribed scatterer density $p: [0, 2\pi) \rightarrow [0, \infty)$, the delay function is given by τ , and $a(\alpha_m, t)$ and $\theta_m(t)$ are stochastic processes for the amplitude and the phase shift of each wave path, respectively.

B. The Amplitude Flip and Phase Shift Processes

To model local shadowing of radio wave paths, we propose an amplitude flip process $a(\alpha, t)$ which flips on when it changes value from 0 to $a^+(\alpha, t) \geq 0$ and flips off when the opposite change occurs. The process $a(\alpha, t)$ thus represents the state of a scatterer, and we will assume that the amplitude function $a^+: [0, 2\pi) \cdot \mathbb{R} \rightarrow [0, \infty)$ is piecewise continuous (it may for example be piecewise constant or depend on the distance from scatterer to receiver). The amplitude process is modeled as a Poisson process with constant flip rate C :

$$P(a(\alpha, \cdot) \text{ flips } k \text{ times within one time step } \Delta t) = \frac{(C\Delta t)^k \exp(-C\Delta t)}{k!}, \quad (6)$$

where flips are independent from the phase shift processes $\{\theta_m(t)\}_{m=1}^M$ and from the scatterers' state $\bigotimes_{m=1}^M \{0, a^+(\alpha_m, t)\}$, with \bigotimes denoting the tensor product. The scatterers' initial state $\{a(\alpha_m, 0)\}_{m=1}^M$ is sampled from the i.i.d. Bernoulli distribution $P(a(\alpha_m, 0) = a^+(\alpha, 0)) = 1/2$ and $P(a(\alpha_m, 0) = 0) = 1/2$ (which is consistent with the steady state distribution as $t \rightarrow \infty$).

The phase shift processes $\{\theta_m(t)\}_{m=1}^M$ are at all times i.i.d. uniform in $[0, 2\pi)$, and the phase of $\theta_m(t)$ is updated by a new sample $\theta_m(t) \sim U[0, 2\pi)$ at every time the scatterer at the angle α_m flips on—as a scatterer flipping on in our model corresponds to a new scatterer appearing at the given angle.

Remark 1: A natural extension of the amplitude process is to make further distinctions between different types of scatterers by also modeling the flip rate as a r.v. The flip rate distribution would then represent additional (possibly infinite) degrees of freedom for adjusting the model signal's frequency spectrum. We do however believe it would be difficult to devise an algorithm that effectively fits the flip rate distribution to measurements. So, for the sake of simplicity, we restrict ourselves here to a model with constant flip rate C .

Remark 2: The presence of measurement noise in the data might be difficult to distinguish from flipping scatterer noise and can affect modeling parameter estimates, such as the flip rate. In this model we make the assumption that measurement noise is negligible relative to the noise generated by flipping scatterers.

C. Related Models

Apart from strong link to Feng and Field's work [4] described in Section I, the flipping scatterers in our MFC model has connections to birth-death modeling of wave paths through Poisson counting processes. In [6] Charalambos *et al.* consider an MFC model that simulates the number of active scatterers by a Poisson counting process. In simplified form the model expresses the low-pass output signal by

$$y(t) = \sum_{i=1}^{N(T)} h_i(t), \quad (7)$$

where $h_i(t)$ denotes i th path's impulse response at time t and $N(T)$ is the Poisson counting process evaluated at a final time $T \geq t$. For each realization, the number of wave paths is fixed to $N(T, \omega)$ in the time span $t \in [0, T]$, so this model does not incorporate the effect of scatterers flipping on and off during the time frame $[0, T]$.

A number of works on indoor channel models have also considered the effects of local wave path shadowing. The occurrence of wave path shadowing in an indoor environment due to human activities is measured in [7], and in [8] a Markov process channel model incorporating birth and death of wave paths is presented. Of particular relevance to our work is the indoor channel model [9], which the authors note is "straight forward extendable to urban environments". It uses a birth and death process with fixed arrival (birth) intensity of scatterers and fixed departure (death) intensity per active scatterer. This is known as an M/M/ ∞ process from queuing theory (having an infinite population of potential scatterers), cf. [10], and it is characterized by the arrival (birth) intensity and departure (death) intensity of scatterers. In comparison, our MFC model has a finite population of scatterers with "rebirths" (with new phase shifts). The stationary distributions of the number of active scatterers will consequently differ, with M/M/ ∞ being Poisson distributed, while the MFC model is binomial ($M, 0.5$) distributed. The impact of this difference will however vanish as the number of scatterers tends to infinity, and the most important aspect for the output signal, which both models capture in a similar way, is the limited life time of a scatterer. Moreover, the life time of a scatterer is exponentially distributed for both models.

Our model may also be linked to the Master Equation for particle dynamics, cf. [11], by considering the of angles of arrival $\{\alpha_m\}_{m=1}^M$ as a lattice with an evolving state space $\otimes_{m=1}^M \{0, a^+(\alpha_m, t)\}$. For a micro-scale lattice populated by finite state spin particles with probabilistic lattice particle dynamics, the time evolution of the state probability mass function satisfies the Master Equation. When the micro-scale state space is large, simulations of lattice particle dynamics are typically very costly. In many settings it is possible to reduce simulation cost by coarse graining (i.e., local averaging) techniques, reducing the size of the state space while preserving essential features of the micro-scale lattice dynamics, cf. [12], [13].

D. The MFC Algorithm

We now present an algorithm for generating signal realizations of the MFC model (5) on a time grid $\mathbf{t} = (t_1, t_2, \dots, t_N)$. The algorithm first generates a lattice of angles of arrival according to the given scattering density and initializes lattice states at time t_1 by assigning phase shift state $\theta_k(t_1)$ and amplitude state $a(\alpha_k, t_1)$ at each of the lattice points. Having fully described the states at t_1 , the signal value $Z_{t_1, M}$ is computed, according to (5). Amplitude and phase shift states are thereafter simulated on the time grid \mathbf{t} and output signal values $Z_{\mathbf{t}, M}$ are computed.

Algorithm 1 The MFC algorithm

Input: Amplitude function a^+ , flip rate C , carrier frequency f_c , scatterer density p , receiver speed v , time grid $\mathbf{t} = (t_1, t_2, \dots, t_N)$.

Output: Signal realization $Z_{\mathbf{t}, M} = (Z_{t_1, M}, Z_{t_2, M}, \dots, Z_{t_N, M})$.

Generate a set of i.i.d. angles of arrival $\{\alpha_k\}_{k=1}^M$ distributed according to the density $p(\alpha)$.

Generate a set of i.i.d. phase shifts $\{\theta_k(0)\}_{k=1}^M$ with $\theta_k(0) \sim U[0, 2\pi)$.

Generate i.i.d. initial state of the amplitudes $\{a(\alpha_k, t_1)\}_{k=1}^M$ from the steady state distribution $P(a(\alpha, t_1) = 0) = P(a(\alpha, t_1) = a^+(\alpha, t_1)) = 1/2$.

Compute $Z_{t_1, M}$ by (5).

for $j = 2$ to N **do**

for $k = 1$ to M **do**

 Generate $n_k \sim \text{Poisson}(C(t_j - t_{j-1}))$ and flip n_k times the state of $a(\alpha_k, t_j)$.

 If $n_k > 0$, update the phase shift process by sampling a new $\theta_k(t_j) \sim U[0, 2\pi)$.

end for

 Compute $Z_{t_j, M}$ by (5).

end for

Remark 3: It is possible to extend the MFC model to scenarios including line of sight wave components. Suppose you have the input/output relation consisting of many diffuse ray contributions in $Z_{\mathbf{t}, M}$ and one line of sight ray with angle of arrival 0° and amplitude V . Then the resulting output signal becomes $Z_{\mathbf{t}, M} + V e^{-i(2\pi f_c \tau(0, t))}$.

III. A STOCHASTIC PROCESS MODEL

In this section we show that the signal $Z_{t,M}$ defined in (5) converges in distribution to a complex Gaussian process as $M \rightarrow \infty$. Thereafter, two algorithms are presented for generating signal realizations from the limit Gaussian process; Algorithms 2 and 3. At the end, the performance of Algorithms 1, 2, and 3 is compared in terms of accuracy and computational cost.

We begin by recalling definitions for circular symmetric multivariate complex normals and circular symmetric Gaussian processes.

A. Definitions and a Convergence Result

Definition 1 (Circular Symmetric Multivariate Complex Normal Distribution): A multivariate complex normal $Z \in \mathbb{C}^n$ is circular symmetric if $e^{i\hat{\theta}}Z$ has the same distribution as Z for any $\hat{\theta} \in \mathbb{R}$. A circular symmetric multivariate complex normal has mean $0 \in \mathbb{C}^n$ and is uniquely described by its covariance matrix $K = \mathbb{E}[ZZ^H]$. We write $Z \sim \mathcal{N}_{\mathbb{C}}(0, K)$, and recall that its probability density function is given by

$$p_Z(z) = \frac{e^{-z^H K^{-1} z}}{\det(K)\pi^N}. \quad (8)$$

Definition 2 (Circular Symmetric Complex Gaussian Process): A complex-valued stochastic process $\{Z_t\}_{t \in [0, T]}$ is a circular symmetric complex Gaussian process if any finite length sample vector $(Z_{t_1}, Z_{t_2}, \dots, Z_{t_n})$ with $0 \leq t_1 \leq t_2 \leq \dots \leq t_n < T$ is multivariate circular symmetric complex normal distributed.

The following theorem shows that $Z_{t,M}$ converges in distribution to a Gaussian process as $M \rightarrow \infty$:

Theorem 1 (Distributional Convergence to a Gaussian Process): Assume the MFC model (5)'s amplitude function $a^+(\cdot, t)$ and delay function $\tau(\cdot, t)$ are both bounded and piecewise continuous on $[0, 2\pi)$ for all times $t \in [0, T]$. Then the signal

$$Z_{t,M} := \frac{1}{\sqrt{M}} \sum_{m=1}^M a(\alpha_m, t) e^{-i(2\pi f_c \tau(\alpha_m, t) + \theta_m(t))} \quad (9)$$

converges in distribution to a circular symmetric complex Gaussian process Z_t as $M \rightarrow \infty$.

Proof: See Appendix A. \blacksquare

B. Algorithms for the Gaussian Process

In this section we present two algorithms for generating realizations of Theorem 1's limit Gaussian process sampled on a time grid $\mathbf{t} = (t_1, t_2, \dots, t_N)$. Since $Z_{\mathbf{t}} = (Z_{t_1}, Z_{t_2}, \dots, Z_{t_N})$ is circular symmetric multivariate complex normal, it is uniquely described by its covariance matrix. By similar computations as in the proof of Theorem 1, we derive that

$$K_{jk} := \text{Cov}(Z_{t_j}, Z_{t_k}) = \frac{e^{-C|t_j - t_k|}}{2} \cdot \int_0^{2\pi} a^+(\alpha, t_j) a^+(\alpha, t_k) e^{i2\pi f_c \Delta\tau(\alpha, t_j, t_k)} p(\alpha) d\alpha. \quad (10)$$

The covariance matrix integral terms (10) are typically not computable, but may be approximated to arbitrary precision by numerical integration:

$$\bar{K}_{jk} = \frac{e^{-C|t_j - t_k|}}{2} \cdot \sum_{\ell=1}^M \underbrace{a^+(x_\ell, t_j) a^+(x_\ell, t_k) e^{i2\pi f_c \Delta\tau(x_\ell, t_j, t_k)} p(x_\ell)}_{=: f(x_\ell)} \nu_\ell, \quad (11)$$

where $0 = x_1 < x_2 < \dots < x_M = 2\pi$ are the quadrature points and ν_ℓ denotes the quadrature weights with the constraint $\sum_{\ell=1}^M \nu_\ell = 2\pi$. For example, if the integrand in (10) is two times differentiable for all $\alpha \in [0, 2\pi)$ except on finite set of identifiable discontinuity points, then the trapezoidal rule

$$\bar{K}_{jk} = \frac{e^{-C|t_j - t_k|}}{2} \sum_{\ell=1}^{M-1} \frac{f(x_\ell) + f(x_{\ell+1})}{2} (x_{\ell+1} - x_\ell), \quad (12)$$

with appropriately chosen quadrature points will yield an approximation error $|K_{jk} - \bar{K}_{jk}| = \mathcal{O}(M^{-2})$, where \mathcal{O} denotes the big O notation. Moreover, if the integrand only is once differentiable for all $\alpha \in [0, 2\pi)$ except on finite set of identifiable discontinuity points, then the rate of convergence is reduced to $|K_{jk} - \bar{K}_{jk}| = \mathcal{O}(M^{-1})$. For a wider study of convergence rates for the trapezoidal rule and Simpson's rule (a higher order quadrature method) applied to low-regularity integrands, see [14].

1) Algorithm 2: We now present a standard way of generating Gaussian process realizations consisting of multiplying the square root of the covariance matrix to a vector of i.i.d. standard complex normals, cf. [10]. The exact covariance matrix K is approximated by the numerically integrated \bar{K} , cf. (11), and the resulting signal realization is denoted $\bar{Z}_{\mathbf{t}} = (\bar{Z}_{t_1}, \bar{Z}_{t_2}, \dots, \bar{Z}_{t_N})$.

Algorithm 2 Covariance matrix based Gaussian process algorithm

Input: Amplitude function a^+ , flip rate C , carrier frequency f_c , scatterer density p , receiver speed v , time grid $\mathbf{t} = (t_1, t_2, \dots, t_N)$.

Output: Signal realization $\bar{Z}_{\mathbf{t}} = (\bar{Z}_{t_1}, \bar{Z}_{t_2}, \dots, \bar{Z}_{t_N})$.

Compute the covariance matrix approximation \bar{K}_{jk} by the numerical integration (11) for $j, k \in \{1, 2, \dots, N\}$.

Singular value decompose $\bar{K} = \bar{U} \bar{S} \bar{U}^H$, and compute $\bar{K}^{-1/2} = \bar{U} \bar{S}^{-1/2}$.

Generate a vector of N i.i.d. standard complex normal elements; $\hat{Z} \sim \mathcal{N}_{\mathbb{C}}(0, I_N)$, and the output signal realization

$$\bar{Z}_{\mathbf{t}} = \bar{K}^{-1/2} \hat{Z}. \quad (13)$$

2) Algorithm 3: Computing the square root of \bar{K} in Algorithm 2 and generating signal realizations by the matrix

vector multiplication (13) are both computationally costly operations. In this section we present an alternative algorithm which in WSS settings improves the efficiency of these operations by circulant-embedding of the covariance matrix and application of the Fast Fourier Transform (FFT). The presentation is adapted from the material in [10, Chapter XI].

We consider the modeling setting

$$\tau(\alpha, t) = -v \cos(\alpha)t/c \quad \text{and} \quad a^+(\alpha, t) = a^+(\alpha). \quad (14)$$

Then the Gaussian process Z_t is a WSS process, which simplifies the structure of the covariance (10) to

$$K_{ij} = \mathbb{E}[Z_{t_i} Z_{t_j}^*] = \frac{e^{-C|t_i - t_j|}}{2} \cdot \int_0^{2\pi} a^+(\alpha)^2 e^{i2\pi f_D \cos(\alpha)(t_i - t_j)} p(\alpha) d\alpha =: A(t_i - t_j), \quad (15)$$

where we recall that $f_D = f_c v/c$ is the maximum Doppler shift and $A(t)$ denotes the autocorrelation function. Sampling the limit Gaussian process Z_t on a uniform time grid $\mathbf{t} = (t_1, t_2, \dots, t_N)$ then yields a circular symmetric multivariate complex normal $Z_{\mathbf{t}}$ with covariance matrix $K \in \mathbb{C}^{N \times N}$ that is Toeplitz, i.e., $K_{i,j} = A(t_i - t_j) =: A_{i-j}$. For Toeplitz matrices, some operations, e.g., roots and matrix vector multiplications, may be computed more efficiently than for general matrices by circulant-embedding. To illustrate the circulant-embedding procedure, let us for simplicity¹ assume $A_{-j} = A_j$, and embed K as the upper left corner of a circulant of order $2N - 2$:

$$\mathcal{C} = \begin{bmatrix} A_0 & A_1 & \cdot & A_{N-1} & A_{N-2} & \cdot & A_2 & A_1 \\ A_1 & A_0 & \cdot & A_{N-2} & A_{N-1} & \cdot & A_3 & A_2 \\ \cdot & \cdot \\ A_{N-1} & A_{N-2} & \cdot & A_0 & A_1 & \cdot & A_{N-3} & A_{N-2} \\ A_{N-2} & A_{N-1} & \cdot & A_1 & A_0 & \cdot & A_{N-4} & A_{N-3} \\ \cdot & \cdot \\ A_1 & A_2 & \cdot & A_{N-1} & A_{N-2} & \cdot & A_1 & A_0 \end{bmatrix}. \quad (16)$$

The circulant matrix \mathcal{C} has the eigendecomposition $\mathcal{C} = F \Lambda F^H$ where F is the finite Fourier matrix of order $2N - 2$ with elements $F_{jk} = e^{i2\pi(j-1)(k-1)/(2N-2)}/\sqrt{2N-2}$, and Λ is the diagonal matrix of eigenvalues $\text{diag}(\Lambda) = F \mathbf{a}$ with $\mathbf{a} = (A_0, A_1, \dots, A_{N-1}, A_{N-2}, \dots, A_2, A_1)^T$. Provided all entries of Λ are non-negative, we may write $\mathcal{C}^{1/2} = F \Lambda^{1/2}$, and a signal realization is generated by $Z_{\mathbf{t}} = R F \Lambda^{1/2} \hat{Z}$, with $\hat{Z} \sim \mathcal{N}_{\mathbb{C}}(0, I_{2N-2})$ and $R: \mathbb{C}^{2N-2} \rightarrow \mathbb{C}^N$ defined by $Rz = (z_1, z_2, \dots, z_N)^T$ for all $z \in \mathbb{C}^{2N-2}$. This leads to the following algorithm for generating WSS signal realizations:

¹See [15] for an instructive description of simulation procedures in the general case when $A_{-j} = A_j^*$ but $A_{-j} \neq A_j$.

Algorithm 3 Covariance based algorithm for WSS processes

Input: Flip rate C , maximum Doppler shift f_D , scatterer density p , uniform time grid $\mathbf{t} = (t_1, t_2, \dots, t_N)$.

Output: Signal realization $\bar{Z}_{\mathbf{t}} = (\bar{Z}_{t_1}, \bar{Z}_{t_2}, \dots, \bar{Z}_{t_N})$.

Compute approximations $\bar{A}_j \approx \bar{K}_{jj}$ by the numerical integration (11) for $j \in \{1, 2, \dots, N\}$.

Determine $\bar{\Lambda}$ by computing $\text{diag}(\bar{\Lambda}) = F(\bar{A}_0, \bar{A}_1, \dots, \bar{A}_{N-1}, \bar{A}_{N-2}, \dots, \bar{A}_2, \bar{A}_1)^T$, using the FFT.

Generate a multivariate complex normal $\hat{Z} \sim \mathcal{N}_{\mathbb{C}}(0, I_{2N-2})$ and use the FFT to compute the output realization $\bar{Z}_{\mathbf{t}} = R F \bar{\Lambda}^{1/2} \hat{Z}$.

C. Error Estimates and Computational Complexity

Three alternative algorithms have been presented for generating signal realizations for the channel model (5), and in this section we will shed some light on when to use which by comparing their performance in terms accuracy and computational cost. We begin by introducing a distance measure for complex-valued random vectors.

Definition 3 (Distance Measure for Complex-Valued Random Vectors): Let X and Y denote two complex-valued random vectors of the same dimension. We define the distributional distance between X and Y to be given by

$$d(X, Y) := \sup_{A \in \mathfrak{C}(\mathbb{C}^N)} |P(X \in A) - P(Y \in A)|, \quad (17)$$

where $\mathfrak{C}(\mathbb{C}^N)$ denotes the class of convex sets in \mathbb{C}^N .

1) *Algorithm 1:* To bound the error of signal realizations generated by Algorithm 1 the following theorem on higher dimensional Berry–Essen bounds will be useful:

Theorem 2 (Bentkus [16]): Let \hat{X}_i be i.i.d. random vectors in \mathbb{R}^N with mean zero and identity covariance matrix and let $X \sim \mathcal{N}(0, I_N)$. Define $S_M := M^{-1/2} \sum_{m=1}^M \hat{X}_m$ and let $\mathfrak{C}(\mathbb{R}^N)$ denote the class of all convex sets in \mathbb{R}^N . Then

$$d(S_M, X) \leq \frac{400N^{1/4} \mathbb{E} \left[|\hat{X}|^3 \right]}{\sqrt{M}}. \quad (18)$$

By applying Theorem 2 we obtain the following upper bound for the approximation error $d(Z_{\mathbf{t},M}, Z_{\mathbf{t}})$:

Corollary 1 (Error bound for Algorithm 1): Let $Z_{\mathbf{t},M}$ denote a signal realization generated by Algorithm 1 with sample times \mathbf{t} restricted to $[0, T)$, and assume the covariance matrix of the corresponding sampled limit Gaussian process $Z_{\mathbf{t}} \sim \mathcal{N}_{\mathbb{C}}(0, K)$, cf. (10), is non-singular so that it may be represented by the singular value decomposition $K = U S U^H$ with $S = \text{diag}(s_i)$, $s_1 \geq s_2 \geq \dots \geq s_N > 0$. Then

$$d(Z_{\mathbf{t},M}, Z_{\mathbf{t}}) \leq \frac{2^{3/4} \cdot 400N^{7/4} \left\| \mathbb{E} \left[(a^+(\alpha, \cdot))^3 \right] \right\|_{L^\infty([0,T])}}{s_N^{3/2} M^{1/2}}. \quad (19)$$

Proof: See Appendix B. ■

To ensure that signal realizations generated by Algorithm 1 fulfills

$$d(Z_{t,M}, Z_t) \leq \text{TOL}, \quad (20)$$

it follows from Corollary 1 that $M = \mathcal{O}(\text{TOL}^{-2} N^{7/2} S_{2N}^{-3})$ scatterers is needed. This yields the computational cost

$$\text{Cost}(\text{Alg. 1}) = \mathcal{O}\left(L \text{TOL}^{-2} \left(\frac{N^{3/2}}{S_{2N}}\right)^3\right), \quad (21)$$

for generating L realizations fulfilling (20).

2) *Algorithm 2*: The error $d(\bar{Z}_t, Z_t)$ between \bar{Z}_t generated by Algorithm 2 and Z_t sampled from the limit Gaussian process can be expressed in terms of the difference between the respective signal realizations' covariance matrices, \bar{K} and K . We recall that this difference is a consequence of approximating the integral terms $K_{j,k}$ of (10) by the numerical integration (11), and that this error takes the bound

$$\max_{1 \leq j, k \leq N} |K_{j,k} - \bar{K}_{j,k}| \leq \epsilon = \mathcal{O}(M^{-\gamma}), \quad (22)$$

where M denotes the number of quadrature points and the convergence rate $\gamma > 0$ depends on the quadrature method used. The following theorem provides an error bound for Algorithm 2.

Theorem 3: Assume the covariance matrix K of the sampled limit Gaussian process Z_t given in (10) is non-singular, so that it may be represented by the singular value decomposition $K = USU^H$ with $S = \text{diag}(s_i)$, $s_1 \geq s_2 \geq \dots \geq s_N > 0$. Let further $\bar{Z}_t \sim \mathcal{N}_C(0, \bar{K})$ be of the same dimension as Z_t , and assume that $\|K - \bar{K}\|_2 \leq N^{1/2}\epsilon$ with $\epsilon = \mathcal{O}(M^{-\gamma})$, $\gamma > 0$, and M chosen so large that $10N^{3/2}\epsilon < s_N$. Then

$$d(\bar{Z}_t, Z_t) = \mathcal{O}\left(\frac{N^{3/2}}{s_N M^\gamma}\right). \quad (23)$$

Proof: See Appendix C. ■

To ensure that signal realizations generated by Algorithm 2 fulfills $d(\bar{Z}_t, Z_t) \leq \text{TOL}$, it follows from Theorem 3 that $M = \mathcal{O}((N^{3/2}/s_N \text{TOL})^{1/\gamma})$ quadrature points is needed. The cost of generating L signal realizations fulfilling the above accuracy constraint thus becomes

$$\text{Cost}(\text{Alg. 2}) = \mathcal{O}\left(N^3 + N^2 \left(\frac{N^{3/2}}{s_N \text{TOL}}\right)^{1/\gamma} + LN^2\right), \quad (24)$$

where $\mathcal{O}(MN^2)$ comes from computing the matrix elements of \bar{K} by quadrature, $\mathcal{O}(N^3)$ comes from computing the square root of \bar{K} , and $\mathcal{O}(LN^2)$ comes from generating L signal realizations.

3) *Algorithm 3*: As for Algorithm 2, signal realizations \bar{Z}_t generated by Algorithm 3 are multivariate circular symmetric complex Gaussian with covariance \bar{K} . Therefore, we may once again use Theorem 3 to conclude that under the assumptions there stated, the cost of generating L signal realizations with

Algorithm 3 fulfilling the accuracy constraint $d(\bar{Z}_t, Z_t) \leq \text{TOL}$ is

$$\text{Cost}(\text{Alg. 3}) = \mathcal{O}\left(N \left(\frac{N^{3/2}}{s_N \text{TOL}}\right)^{1/\gamma} + LN \log(N)\right), \quad (25)$$

where $\mathcal{O}(MN)$ comes from computing the covariance elements $\{\bar{A}_j\}_{j=-N+1}^{N-1}$ of \bar{K} by quadrature, $\mathcal{O}(N \log(N))$ comes from computing the spectral decomposition $\bar{\Lambda}$, and $\mathcal{O}(LN \log(N))$ comes from generating L signal realizations using FFT.

4) *Summary of the Complexity Estimates*: We now summarize the derived upper bounds for the computational cost of generating output realizations for Algorithms 1, 2, and 3. Let us however stress that the obtained error bounds, on which the cost estimates are based, are not proven to be sharp, so some bounds may be conservative. In Table I we present cost estimates for general modeling settings that may include having time dependent amplitude functions a^+ and/or non-linear delay functions $\tau(\alpha, t)$. The results of the table indicate that when the quadrature convergence rate $\gamma \geq 3/5$, cf. (22), the covariance based Gaussian process algorithm, Algorithm 2, is asymptotically the most efficient algorithm; and this will hold for a large class of problem settings: For the trapezoidal rule, for example, integrands in (10) which are once differentiable except at a finite, identifiable number of discontinuity points will have the rate $\gamma = 1$, cf. Section III-B.

In Table II we compare the algorithms' performance in the WSS setting (14). The table shows that at least when the quadrature convergence rate $\gamma \geq 1/2$, Algorithm 3 is the asymptotically most efficient.

See Fig. 6 for a runtime comparison of the algorithms in a WSS setting, and [1] for a more elaborate study of the above cost bounds.

IV. APPLICATIONS OF THE POWER SPECTRAL DENSITY

The shape of the PSD depends on both the MFC model's flip rate and the scatterer density. Restricting ourselves to the WSS setting (14), we will in this section describe a method for estimating the flip rate C from the PSD computed from real life signal measurements.

A. Introduction

The PSD is given by $S_C(f) = \mathcal{F}\{A(\cdot)\}$, where $A(t)$ is the autocorrelation of the limit complex Gaussian process Z_t , $\mathcal{F}(\cdot)$ denotes the Fourier Transform, and the subscript C in S_C denotes the PSD's dependence on the flip rate. In the WSS setting (14), it follows from (15) and by using the Convolution Theorem for Fourier transforms that

$$S_C(f) = \int_0^{2\pi} \frac{C(a^+(\alpha))^2 p(\alpha)}{C^2 + (2\pi(f - f_D \cos(\alpha)))^2} d\alpha. \quad (26)$$

See [4], for more details on a derivation of a similar PSD expression.

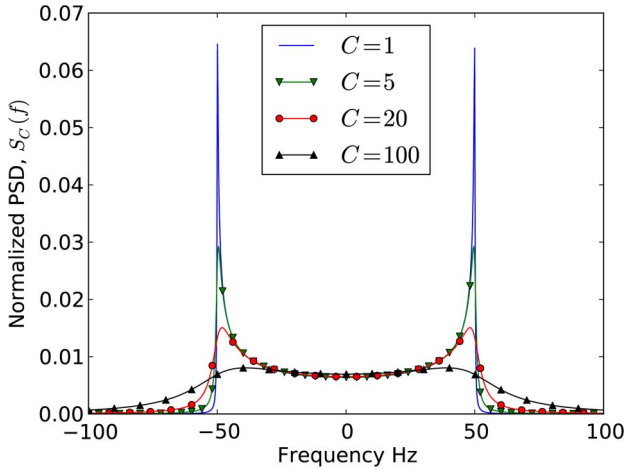


Fig. 2. The PSD function $S_C(f)$ is plotted for different flip rate values C in the setting $f_D = 50$ Hz and $(a^+)^2 p = (2\pi)^{-1}$.

From (26) we see that $S_C(f)$ depends on the flip rate C and the term $(a^+)^2 p$, which we hereafter refer to as a scaled scatterer density. Fig. 2 illustrates $S_C(f)$'s dependency on the flip rate C in the modeling setting $(a^+)^2 p = (2\pi)^{-1}$ with $S_0(f)$ equaling Jakes' spectrum and $S_C(f)$ becoming a progressively mollified version of Jakes' spectrum the higher value C takes.

B. A link to Feng and Field's Model

In the WSS setting (14) Feng and Field's extension of Clarke's model that we described in equation (3) have very similar signal autocorrelation and PSD to our proposed MFC model. For Feng and Field's model the autocorrelation function becomes

$$E[\varepsilon_t \varepsilon_0^*] = \sum_{m=1}^M E[a_m^2] e^{-B|t|/2} \int_0^{2\pi} e^{i2\pi f_D \cos(\alpha)t} d\alpha, \quad (27)$$

while we recall that our model's autocorrelation is in the given setting on the form

$$E[Z_t Z_0^*] = \frac{e^{-C|t|}}{2} \int_0^{2\pi} (a^+(\alpha))^2 e^{i2\pi f_D \cos(\alpha)t} p(\alpha) d\alpha, \quad (28)$$

cf. (15). It should be noted that this similarity is obtained although modeling assumptions are quite different: in our model the wave path amplitudes are governed by Poisson flip processes, whereas Feng and Field's model has time invariant amplitude functions; in our model phases are updated when scatterers flips on, whereas Feng and Field's model phases evolve as scaled Wiener processes. The similarity between the models is intriguing, but it should not be exaggerated. After all, there are more degrees of freedom in ours (C and $(a^+)^2 p$) than in theirs (only B), and the WSS modeling setting (14) is only one of many possible settings for our model, while it is the only possible setting for theirs.

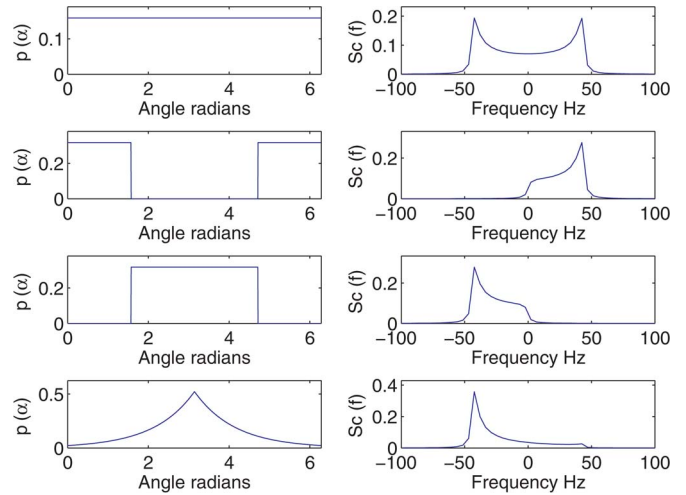


Fig. 3. Right column plots illustrate the PSD $S_C(f)$ obtained by (26) when the scaled scatterer density $(a^+)^2 p(\alpha)$ is given by respective left column plots, $C = 10$, and $f_D = 50$. **Top row:** $(a^+)^2 p = 1/(2\pi)$ yields the mollified Jakes' spectrum PSD. **Second row:** $(a^+)^2 p(\alpha) = 1_{[-\pi/2, \pi/2]}(\alpha)/\pi$ yields a PSD consisting almost exclusively of positive Doppler shifts since the receiver's moves towards the active scatterers. **Third row:** $(a^+)^2 p(\alpha) = 1_{[\pi/2, 3\pi/2]}(\alpha)/\pi$ yields a PSD consisting almost exclusively of negative Doppler shifts since the receiver moves away from the active receivers. **Last row:** $(a^+)^2 p(\alpha) = \exp(-|\alpha - \pi|)/2$.

C. Model Parameter Estimation From PSD Measurements

Feng and Field's publication [4] further presents a method for estimating the flip rate constant C from measurements which can be used when the scaled scatterer density $(a^+)^2 p$ is known. Namely, given a measurement of the PSD, $\hat{S}(f)$, estimate C through minimizing the distance between the theoretical and measured spectra by

$$C = \arg \min_{x>0} \cos^{-1} \left(\int_{\mathbb{R}} \sqrt{\hat{S}(f) S_x(f)} df \right), \quad (29)$$

where the PSD are scaled so that $\|\hat{S}\|_2 = 1$ and $\|S_x\|_2 = 1$. However, from (26) we see that the shape of the PSD depends both on the flip rate and the scaled scatterer density on $(a^+)^2 p$. In Fig. 3, we shed some light on the relationship between $(a^+)^2 p$ and the PSD, with the most notable property being that if the receiver moves towards the region where $(a^+)^2 p$ has most of its mass, then the PSD will generally be higher-valued for positive frequencies than for negative frequencies, and oppositely if the receiver moves away from the region where $(a^+)^2 p$ has most of its mass. So to estimate the flip rate from PSD measurements using equation (29), $(a^+)^2 p$ either has to be known or estimated. It is however a much more difficult and costly task to estimate $(a^+)^2 p$ than the flip rate, as $(a^+)^2 p$ represents an infinite degrees of freedom, so we restrict ourselves to a tentative approach here. Let \hat{S} denote a real life PSD measurement for a moving receiver, and consider relation (26) as the inhomogeneous Fredholm integral equation

$$\int_0^{2\pi} \mathcal{K}_C(f, \alpha) (a^+(\alpha))^2 p(\alpha) d\alpha = \hat{S}(f), \quad (30)$$

with unknown $(a^+(\alpha))^2 p(\alpha)$ and parameterized by the flip rate C . For a fixed flip rate, one may approach this problem by discretization, which leads to a system of linear equations, and, supposing the measurement \hat{S} is noisy, solve the inverse problem using Tikhonov regularization or similar techniques, cf. [17].

V. NUMERICAL EXAMPLES

In this section we present three numerical examples for studying the performance of the presented algorithms. The first example considers a WSS modeling setting and study how well our models' PSD and autocorrelation can reproduce those of a real signal measurement by optimal fitting of the flip rate C . The second example compares the computational cost of numerical signal generation by Algorithms 1, 2, and 3, and in the last example we study the effect the time variation has on the statistics of the channel model in a non-stationary channel environment setting.

A. Example 1

We consider the WSS modeling setting (14) with

$$(a^+)^2 p(\alpha) = \mathbb{1}_{0.35 < |\alpha| < 2.8} \sum_{i=1}^9 b_i e^{-\hat{c}_i ||\alpha| - \hat{\alpha}_i|} + \mathbb{1}_{1.7 < |\alpha| < 2} \frac{7}{5}, \tag{31}$$

where $\mathbb{1}$ denotes the indicator function, $\alpha \in (-\pi, \pi)$ and

$$\begin{aligned} b &= (39, 31, 3, 11, 18.5, 6.5, 10, 6, 4), \\ \hat{c} &= (10, 38, 40, 40, 30, 12, 22, 30, 14), \\ \hat{\alpha} &= (0.385, 0.73, 0.95, 1.06, 1.19, 1.57, 2.07, 2.23, 2.48). \end{aligned} \tag{32}$$

The scaled scatterer density (31) is composed of basis functions of the kind $\mathbb{1}_{\hat{a} < |\alpha| < \hat{b}}$ and $e^{-\hat{c}|\alpha - \hat{\alpha}|}$ and the parameter vectors (32) are fitted to the signal measurement by trial and error until our model's PSD and autocorrelation functions are close to those of the measured signal. (See Fig. 3 for illustrations of how the PSD for these kinds of basis functions may look.) The other model parameters are the delay function $\tau(\alpha, t) = -v \cos(\alpha)t/c$, the receiver velocity $v = 12.5$ m/s and the carrier frequency $f_c = 1.8775$ GHz. A measured signal, sampled uniformly on the time interval $[0, 0.16]$ using $N = 1419$ samples, is provided by Henrik Asplund from Ericsson Research, who did the measurement in the urban neighborhood of Kiista, Stockholm. The PSD of the measured signal \hat{Z}_t is computed by the FFT of $\hat{Z}_t \hat{Z}_0^* =: \hat{S}(f)$, and to remove the measurement noise an ideal low-pass filter with cut-off frequency 500 Hz is applied to $\hat{S}(f)$. The model flip rate C is thereafter fitted to the measurement by minimizing (29), with resulting best fit $C \approx 3.9027$. See Fig. 4 for a comparison of the theoretical PSD S_C and the measurement PSD \hat{S} . Having determined the flip rate, signal realizations are generated by the MFC algorithm, each containing $M = 2000$ wave paths. For the Gaussian process algorithms $M = 1000$ quadrature points are used to compute the covariance matrix \bar{K}_{jk} by the

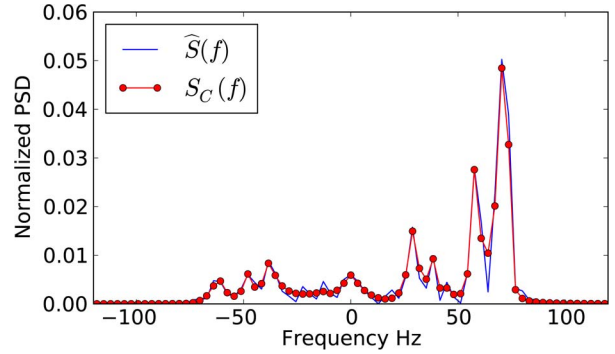


Fig. 4. The best fit of $S_C(f)$ to a single measured signal's PSD $\hat{S}(f)$. The fitting is done by (29).

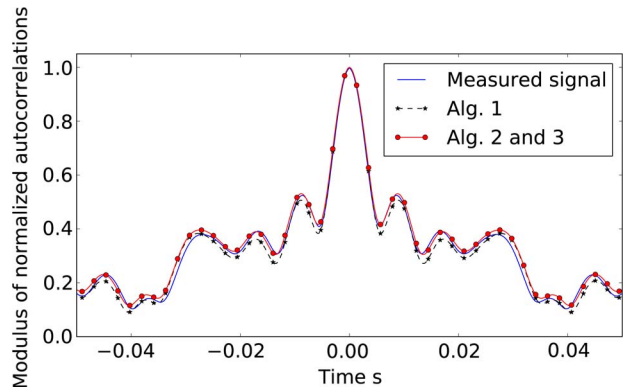


Fig. 5. Comparison of the modulus of the normalized autocorrelation of the signal measurement and the fitted model's signal realizations generated by Algorithms 1, 2, and 3.

trapezoidal rule (12). As an additional measure of the difference between our model and the signal measurement, respective autocorrelations are plotted in Fig. 5. Here, the autocorrelation of the measured signal and signal realizations of Algorithm 1 are computed using the MATLAB function `xcorr.m` (taking the average autocorrelation of $L = 2000$ signal realizations for Algorithm 1), while the autocorrelation for Algorithms 2 and 3 already is computed in the covariance matrix \bar{K} .

B. Example 2

We next compare the computational runtime cost of generating numerical signal realizations using Algorithms 1, 2, and 3 over the time interval $[0, 0.1]$ using $N = 1000$ time steps. We consider the WSS modeling setting (14) with

$$(a^+)^2 p(\alpha) = (|\alpha - \pi|^5 + |\alpha|^3) \mathbb{1}_{[0.3, 2.6]}(|\alpha|), \tag{33}$$

the maximum Doppler shift $f_D = 50$ Hz and flip rate $C = 5$. For the MFC algorithm $M = 2000$ wave paths are used in the simulations, while for Algorithms 2 and 3 we use $M = 1000$ quadrature points to compute the Toeplitz covariance matrix \bar{K}_{jk} by the trapezoidal rule (12). Fig. 6 gives the complete runtime cost of generating up to $L = 40\,000$ i.i.d. signal realizations using the MATLAB numerical computing environment on an Intel Xeon CPU X5550, 2.67 GHz architecture.

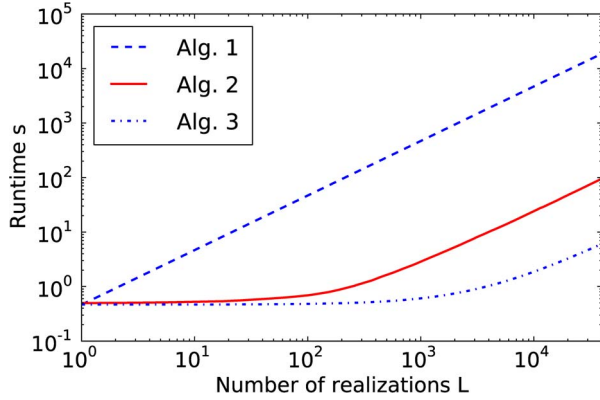


Fig. 6. Comparison of the runtime of generating up to $L = 40\,000$ i.i.d. signal realizations for the channel environment described in Example V-B.

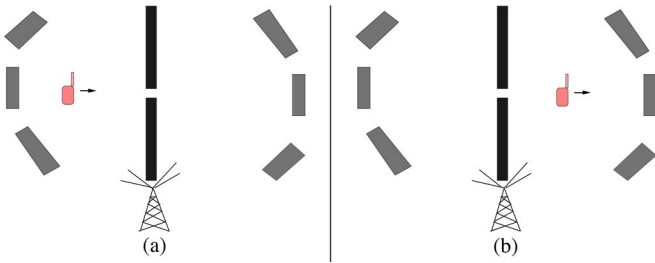


Fig. 7. A receiver moving rightwards through a thin opening in a non-scattering (black) wall and thereby experiencing a change in the scattering environment.

C. Example 3

In the third example we model the time-varying scattering environment with a receiver moving from left to right through a thin opening in a non-reflecting black wall, as sketched in Fig. 7. When the mobile receiver is on the left side of the opening, it only receives wave paths from the reflecting gray walls at its rear; and when it is on the right side of the opening, it only receives wave paths from the reflecting gray walls in front of it. We consider the time interval $[0, 2)$ seconds and assume the following instant change in the amplitude function as the receiver moves through the black wall's opening at $t = 1$:

$$a^+(\alpha, t) = \begin{cases} \cos^2(\alpha) \mathbb{1}_{|\alpha| \geq \pi/2}, & \text{for } 0 \leq t < 1, \\ \cos^2(\alpha) \mathbb{1}_{|\alpha| \leq \pi/2}, & \text{for } 1 \leq t < 2, \end{cases} \quad (34)$$

for angles of arrival $\alpha \in (-\pi, \pi)$. This represents a scattering environment where the amplitude flip process, modeled as due to local shadowing, is a non-stationary process. Other modeling parameters are as follows: $p = (2\pi)^{-1}$, $C = 5$, and $f_D = 50$ Hz. Fig. 8 contains snapshots of the time dependent PSD for a single stochastic signal realization created by Algorithm 2, showing that when the mobile receiver is situated on the left side of the opening, the PSD is concentrated around $-f_D$, and when the receiver is on the right side of the opening, the PSD is concentrated around f_D . By the discussion in Section IV on the relation between $(a^+)^2 p$ and $S_C(f)$, the snapshot PSD in Fig. 8 seem reasonable.

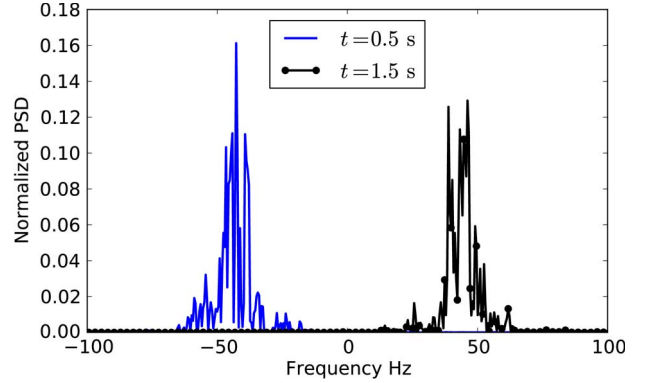


Fig. 8. Snapshots of the time dependent PSD for a signal realization at $t = 0.5$ s when the receiver is situated on the left side of the wall opening (blue line) and at $t = 1.5$ s situated at to the right side of the wall opening (green line).

VI. CONCLUSION

In this paper, we have presented an MFC model extension of Clarke's model that incorporates time-varying randomness through stochastic amplitude processes $a(\alpha_m, t)$ that flip on and off. For the purpose of lowering the computational cost of generating signal realizations we showed that in the limit when the number of active scatterers tends to infinity, the MFC model signal converges in distribution to a Gaussian process. Three algorithms were presented for generating stochastic signal realizations; one for the MFC model and two for the limit Gaussian process. By rigorous analysis and numerical studies we have shown that in many settings the Gaussian process algorithms will generate signal realizations orders of magnitude faster than the MFC model's algorithm. Further numerical examples illustrate how model parameters may be fitted to real signal measurements and that the model is applicable even in non-stationary settings.

The developed MFC and Gaussian process models are 2D models, and for many scattering environments the reduced dimensionality is a reasonable simplification. But for environments with nontrivial 3D scattering densities it is of course not. Expansion to 3D and more detailed studies of the channel statistics in non-stationary settings are potential future extensions of this work.

APPENDIX A PROOF OF THEOREM 1

The following definition of the multivariate complex normal distribution will be useful in the proof of Theorem 1.

Definition 4 (Multivariate Complex Normal Distribution): A random vector $Z = (Z_1, Z_2, \dots, Z_n) \in \mathbb{C}^n$ is said to be complex multivariate normal distributed if the linear combination of its components, $\mathbf{c}^H Z \in \mathbb{C}^1$ is complex normal distributed for all $\mathbf{c} \in \mathbb{C}^n$.

Proof of Theorem 1: Definitions 4 and 2 imply that if the sum

$$\Upsilon_{\mathbf{t}, \mathbf{c}, M} := \sum_{i=1}^n c_i^* Z_{t_i, M}, \quad (35)$$

converge in distribution to a complex normal for any finite length set of sampling times $\mathbf{t} = (t_1, t_2, \dots, t_n) \subset [0, T]$ and $\mathbf{c} = (c_1, c_2, \dots, c_n) \in \mathbb{C}^n$, then $Z_{\mathbf{t}, M}$ converges in distribution to a complex Gaussian process on $[0, T]$. By the aid of the Central Limit Theorem (CLT) we prove that this holds by showing that for any \mathbf{t} and \mathbf{c} , an equality on the form

$$\Upsilon_{\mathbf{t}, \mathbf{c}, M} = \frac{1}{\sqrt{M}} \sum_{m=1}^M \xi_m, \quad (36)$$

holds, with ξ_1, ξ_2, \dots being a sequence of i.i.d. circular symmetric² with bounded variance.

We begin by rewriting (35) as a sum of M i.i.d. random variables:

$$\Upsilon_{\mathbf{t}, \mathbf{c}, M} = \frac{1}{\sqrt{M}} \sum_{m=1}^M \underbrace{\sum_{j=1}^n c_j^* a(\alpha_m, t_j) e^{-i(2\pi f_c \tau(\alpha_m, t_j) + \theta_m(t_j))}}_{=: \xi_m} \quad (37)$$

Since both $\{\theta_m(\cdot)\}_m$, $\{a(\alpha_m, \cdot)\}_m$ are i.i.d. and mutually independent, it straightforwardly follows that ξ_m is circular symmetric. To further compute the variance of ξ_m , we first need to derive some useful properties. By the definition of the phase shift processes and amplitude process given in Section II-B, $P(\theta_m(t_j) = \theta_m(t_k)) = \exp(-C|t_j - t_k|)$ and

$$\begin{aligned} & \mathbb{E}[a(\alpha_m, t_j)a(\alpha_m, t_k) | \alpha_m, \theta_m(t_j) = \theta_m(t_k)] \\ &= a^+(\alpha_m, t_j)a^+(\alpha_m, t_k)P(a(\alpha_m, t_j) = a^+(\alpha_m, t_j)) \\ &= \frac{a^+(\alpha_m, t_j)a^+(\alpha_m, t_k)}{2}. \end{aligned} \quad (38)$$

Introducing the short-hand notation $\Delta\tau(\alpha, s, t) := \tau(\alpha, t) - \tau(\alpha, s)$ and $\Delta\theta_m(s, t) := \theta_m(t) - \theta_m(s)$, we see that

$$\begin{aligned} & \mathbb{E} \left[a(\alpha_m, t_j)a(\alpha_m, t_k) e^{i(2\pi f_c \Delta\tau(\alpha_m, t_j, t_k) + \Delta\theta_m(t_j, t_k))} \middle| \alpha_m \right] \\ &= \mathbb{E} [a(\alpha_m, t_j)a(\alpha_m, t_k) | \alpha_m, \theta_m(t_j) = \theta_m(t_k)] \\ & \quad \cdot e^{i2\pi f_c \Delta\tau(\alpha_m, t_j, t_k)} P(\theta_m(t_j) = \theta_m(t_k)) \\ &= e^{-C|t_j - t_k|} \frac{a^+(\alpha_m, t_j)a^+(\alpha_m, t_k)}{2} e^{i2\pi f_c \Delta\tau(\alpha_m, t_j, t_k)}, \end{aligned} \quad (39)$$

which gives the variance

$$\begin{aligned} \sigma_\xi^2 &:= \mathbb{E}[|\xi_1|^2] = \sum_{j,k=1}^n c_j^* c_k \frac{e^{-C|t_j - t_k|}}{2} \\ & \quad \cdot \int_0^{2\pi} a^+(\alpha, t_j)a^+(\alpha, t_k) e^{i2\pi f_c \Delta\tau(\alpha, t_j, t_k)} p(\alpha) d\alpha. \end{aligned} \quad (40)$$

We have shown that $\Upsilon_{\mathbf{t}, \mathbf{c}, M}$ is a scaled sum of i.i.d. circular symmetric random variables ξ_m with bounded variance. It then follows by the CLT (for complex-valued random variables)

²A complex-valued r.v. X is circular symmetric if $e^{i\hat{\theta}}X$ has the same distribution as X for any $\hat{\theta} \in \mathbb{R}$.

$\Upsilon_{\mathbf{t}, \mathbf{c}, M}$ converge in distribution to $\mathcal{N}_{\mathbb{C}}(0, \sigma_\xi^2)$ as $M \rightarrow \infty$. By Definition 4, this implies that $Z_{\mathbf{t}, M}$ converge in distribution to a complex Gaussian process $Z_{\mathbf{t}}$ as $M \rightarrow \infty$. Moreover, since the sample vector $(Z_{t_1, M}, Z_{t_2, M}, \dots, Z_{t_n, M})$ is circular symmetric for any set of sampling times $\mathbf{t} = (t_1, t_2, \dots, t_n) \subset [0, T]$, $Z_{\mathbf{t}}$ is also circular symmetric. ■

APPENDIX B

PROOF OF COROLLARY 1

Proof: Since $Z_{\mathbf{t}}$ is a circular symmetric complex normal, the equation

$$\begin{aligned} & P(Z_{\mathbf{t}, M} \in A) - P(Z_{\mathbf{t}} \in A) \\ &= P\left((K/2)^{-1/2} Z_{\mathbf{t}, M} \in \tilde{A}\right) - \int_{\tilde{A}} \frac{e^{-|z|^2/2}}{(2\pi)^N} dz, \end{aligned} \quad (41)$$

holds for any set $A \in \mathfrak{C}(\mathbb{C}^N)$, where $\tilde{A} := (K/2)^{-1/2}A$. The linearly transformed signal $(K/2)^{-1/2}Z_{\mathbf{t}, M}$ may be written

$$(K/2)^{-1/2}Z_{\mathbf{t}, M} = \frac{1}{\sqrt{M}} \sum_{m=1}^M (K/2)^{-1/2} \check{Z}_m \quad (42)$$

with i.i.d. complex-valued random vectors

$$\check{Z}_m := \begin{bmatrix} a(\alpha_m, t_1) \exp(-i(2\pi f_c \tau(\alpha_m, t_1) + \theta_m(t_1))) \\ a(\alpha_m, t_2) \exp(-i(2\pi f_c \tau(\alpha_m, t_2) + \theta_m(t_2))) \\ \vdots \\ a(\alpha_m, t_N) \exp(-i(2\pi f_c \tau(\alpha_m, t_N) + \theta_m(t_N))) \end{bmatrix}. \quad (43)$$

Following the proof of Theorem 1, \check{Z}_m is circular symmetric with covariance matrix K given by (10). The associated $2N$ -dimensional real-valued random vector $(\text{Re}((K/2)^{-1/2}\check{Z}_m), \text{Im}((K/2)^{-1/2}\check{Z}_m))$ has mean 0 and identity covariance I_{2N} , and by Hölder's inequality,

$$\begin{aligned} & \mathbb{E} \left[\left| (K/2)^{-1/2} \check{Z}_m \right|^3 \right] \leq \frac{2^{3/2}}{s_N^{3/2}} \mathbb{E} \left[\left(\sum_{j=1}^N (a(\alpha, t_j))^2 \right)^{3/2} \right] \\ & \leq 2^{1/2} \left(\frac{N}{s_N} \right)^{3/2} \left\| \mathbb{E} \left[(a^+(\alpha, \cdot))^3 \right] \right\|_{L^\infty([0, T])}. \end{aligned} \quad (44)$$

The proof is concluded by applying Theorem 2. ■

APPENDIX C

PROOF OF THEOREM 3

The following corollary will be used in the proof of Theorem 3:

Corollary 2 [18, p. 198]: Let G and F be arbitrary matrices (of the same size) where $\sigma_1 \geq \dots \geq \sigma_n$ are the singular values of G and $\sigma'_1 \geq \dots \geq \sigma'_n$ are the singular values of $G + F$. Then $|\sigma_i - \sigma'_i| \leq \|F\|_2$.

Proof of Theorem 3: By the theorem's assumptions, we may write $\bar{K} = K + \delta K$ with $\|\delta K\|_2 \leq N^{1/2}\epsilon$, and since \bar{K} is symmetric, it has a singular value decomposition $\bar{K} = \bar{U} \bar{S} \bar{U}^H$ with $\bar{s}_1 \geq \bar{s}_2 \geq \dots \geq \bar{s}_N \geq 0$. By Corollary 2, we have that $\max_{1 \leq j \leq N} |s_j - \bar{s}_j| \leq N^{1/2}\epsilon < s_N$. This further implies that $\bar{s}_N > 0$, so \bar{K} is non-singular and its inverse can be represented by

$$\begin{aligned} \bar{K}^{-1} &= (K + \delta K)^{-1} = (I + K^{-1}\delta K)^{-1}K^{-1} \\ &= K^{-1} + \sum_{j=1}^{\infty} (-K^{-1}\delta K)^j K^{-1}. \end{aligned} \quad (45)$$

Moreover, by the assumption of M being sufficiently large,

$$\left\| K^{1/2} \sum_{j=1}^{\infty} (-K^{-1}\delta K)^j K^{-1/2} \right\|_2 \leq \frac{2N^{1/2}\epsilon}{s_N}. \quad (46)$$

For all Borel sets $A \subset \mathbb{C}^N$, we derive the following upper bound

$$\begin{aligned} &P(\bar{Z}_t \in A) - P(Z_t \in A) \\ &= \frac{1}{\pi^N |\det(K)|} \int_A \frac{e^{-z^H \bar{K}^{-1} z}}{|\det(K^{-1} \bar{K})|} - e^{-z^H K^{-1} z} dz \\ &= \frac{1}{\pi^N |\det(K)|^{1/2}} \int_A e^{-z^H K^{-1} z} \\ &\quad \cdot \left(\frac{e^{-z^H \sum_{j=1}^{\infty} (-K^{-1}\delta K)^j K^{-1} z}}{|\det(K^{-1} \bar{K})|} - 1 \right) dz \\ &= \frac{1}{(2\pi)^N} \int_{(K/2)^{-1/2} A} e^{-|z|^2/2} \\ &\quad \cdot \left(\frac{e^{-z^H K^{1/2} \sum_{j=1}^{\infty} (-K^{-1}\delta K)^j K^{-1/2} z/2}}{|\det(K^{-1} \bar{K})|} - 1 \right) dz \\ &\stackrel{(46)}{\leq} \frac{1}{(2\pi)^N} \int_{(K/2)^{-1/2} A} e^{-|z|^2/2} \\ &\quad \cdot \left(\frac{e^{(N^{1/2}\epsilon/s_N)|z|^2}}{\prod_{j=1}^N (1 - N^{1/2}\epsilon/s_j)} - 1 \right) dz \\ &\leq \frac{1}{(2\pi)^N} \int_{\mathbb{R}^{2N}} e^{-|x|^2/2} \\ &\quad \cdot \left(\left(1 - \frac{N^{1/2}\epsilon}{s_N}\right)^{-N} e^{(N^{1/2}\epsilon/s_N)|x|^2} - 1 \right) dx \\ &= \left(1 - \frac{N^{1/2}\epsilon}{s_N}\right)^{-N} \left(1 - 2\frac{N^{1/2}\epsilon}{s_N}\right)^{-N} - 1 \\ &\leq e^{10N^{3/2}\epsilon/s_N} - 1 \leq \frac{20N^{3/2}\epsilon}{s_N}. \end{aligned} \quad (47)$$

Here, we used that if \hat{X} is a $2N$ -dimensional real-valued multivariate normal with mean zero and identity covariance matrix,

then $E[e^{t|\hat{X}|^2}] = (1 - 2t)^{-N}$ is the moment generating function to a chi-square distributed variable with $2N$ degrees of freedom. Calculating along the same lines one obtains a similar lower bound $P(\bar{Z}_t \in A) - P(Z_t \in A) \geq -3N^{3/2}\epsilon/s_N$. The upper and lower bounds are both valid for the class of all Borel sets $A \in \mathbb{C}^N$, and this class contains the class of convex sets $\mathfrak{C}(\mathbb{C}^N)$.

ACKNOWLEDGMENT

The authors would like to thank Prof. Anders Szepessy for fruitful discussions and Henrik Asplund at Ericsson Research for providing signal measurements and modeling extension ideas. They would also like to thank the four reviewers for the many valuable comments and suggestions, which has helped improve this paper considerably. This work is an updated version of the technical report [1] in the Ph.D. thesis [2].

REFERENCES

- [1] H. Hoel and H. Nyberg, "Gaussian coarse graining of a master equation extension of Clarke's model," Numer. Anal. (NA), KTH, Stockholm, Sweden, Tech. Rep. 2012:5, 2012.
- [2] H. Hoel, "Complexity and error analysis of numerical methods for wireless channels, SDE, random variables and quantum mechanics," Ph.D. dissertation, Numer. Anal. (NA), KTH, Stockholm, Sweden, 2012.
- [3] R. H. Clarke, "A statistical theory of mobile-radio reception," *Bell Sys. Tech.*, vol. 47, no. 6, pp. 957–1000, Jul./Aug. 1968.
- [4] T. Feng and T. Field, "Statistical analysis of mobile radio reception: An extension of Clarke's model," *IEEE Trans. Commun.*, vol. 56, no. 12, pp. 2007–2012, Dec. 2008.
- [5] T. Feng, T. Field, and S. Haykin, "Stochastic differential equation theory applied to wireless channels," *IEEE Trans. Commun.*, vol. 55, no. 8, pp. 1478–1483, Aug. 2007.
- [6] C. D. Charalambous, S. M. Djouadi, and C. Kourtellis, "Statistical analysis of multipath fading channels using generalizations of shot noise," *EURASIP J. Wireless Commun. Netw.*, vol. 2008, no. 1, pp. 186020–1–186020–9, Jul. 2008.
- [7] I. Kashiwagi, T. Taga, and T. Imai, "Time-varying path-shadowing model for indoor populated environments," *IEEE Trans. Veh. Technol.*, vol. 59, no. 1, pp. 16–28, Jan. 2010.
- [8] C.-C. Chong *et al.*, "A novel wideband dynamic directional indoor channel model based on a Markov process," *IEEE Trans. Wireless Commun.*, vol. 4, no. 4, pp. 1539–1552, Jul. 2005.
- [9] T. Zwick, C. Fischer, and W. Wiesbeck, "A stochastic multipath channel model including path directions for indoor environments," *IEEE J. Sel. Areas Commun.*, vol. 20, no. 6, pp. 1178–1192, Aug. 2002.
- [10] S. Asmussen and P. W. Glynn, *Stochastic Simulation: Algorithms and Analysis*, vol. 57. New York, NY, USA: Springer-Verlag, 2007, ser. Stochastic Modelling and Applied Probability.
- [11] N. G. van Kampen, *Stochastic Processes in Physics and Chemistry*, vol. 888. Amsterdam, The Netherlands: North-Holland, 1981, ser. Lecture Notes in Mathematics.
- [12] M. A. Katsoulakis, A. J. Majda, and D. G. Vlachos, "Coarse-grained stochastic processes and Monte Carlo simulations in lattice systems," *J. Comput. Phys.*, vol. 186, no. 1, pp. 250–278, Mar. 2003.
- [13] M. A. Katsoulakis and A. Szepessy, "Stochastic hydrodynamical limits of particle systems," *Commun. Math. Sci.*, vol. 4, no. 3, pp. 513–549, 2006.
- [14] D. Cruz-Uribe and C. J. Neugebauer, "Sharp error bounds for the trapezoidal rule and Simpson's rule," *J. Inequal. Pure Appl. Math.*, vol. 3, no. 4, p. 22, 2002, Article 49.
- [15] D. B. Percival, "Exact simulation of complex-valued Gaussian stationary processes via circulant embedding," *Signal Process.*, vol. 86, no. 7, pp. 1470–1476, Jul. 2006.
- [16] V. Bentkus, "On the dependence of the Berry–Esseen bound on dimension," *J. Stat. Plan. Infer.*, vol. 113, no. 2, pp. 385–402, May 2003.
- [17] C. R. Vogel, *Computational Methods for Inverse Problems*, vol. 23. Philadelphia, PA, USA: SIAM, 2002, ser. Frontiers in Applied Mathematics.
- [18] J. W. Demmel, *Applied Numerical Linear Algebra*. Philadelphia, PA, USA: SIAM, 1997.



Håkon Hoel was born in Oslo, Norway, in 1980. He received the M.Sc. degree in computational science from the University of Oslo, Oslo, Norway, in 2006 and the Ph.D. degree in numerical analysis from the Royal Institute of Technology (KTH), Stockholm, Sweden, in 2012.

He is currently a Postdoctoral Researcher with the Stochastic Numerics Research Group, King Abdulah University of Science and Technology, Thuwal, Saudi Arabia. His main research interests are applications of stochastic processes in channel modeling,

adaptive numerical integration methods for stochastic differential equations, and analysis of and development of algorithms for multilevel Monte Carlo methods.



Henrik Nyberg was born in Jönköping, Sweden, in 1963. He received the M.Sc. degree in engineering physics and the Ph.D. degree in mathematical statistics from Chalmers Technical University, Gothenburg, Sweden, in 1987 and 1993, respectively.

Since 1993, he has been with Ericsson AB, Stockholm, Sweden. As a Researcher at Ericsson, he has conducted research on teletraffic modeling, load control, and radio resource management in wireless networks. His research interests span over simulation and stochastic modeling of traffic, wireless networks,

complex city environments, and radio propagation.